Hadronic vacuum polarization for the muon $g-2$ from lattice QCD: long-distance and full light-quark connected contribution

Alexei Bazavov,[1] Claude W. Bernard,[2] David A. Clarke,[3] Christine Davies,[4] Carleton DeTar,[3] Aida X. El-Khadra,[5,6] Elvira Gámiz,[7] Steven Gottlieb,[8] Anthony V. Grebe,[9] Leon Hostetler,[8] William I. Jay,[10] Hwancheol Jeong,[8] Andreas S. Kronfeld,[9] Shaun Lahert,[3,*] Jack Laiho,[11] G. Peter Lepage,[12] Michael Lynch,[5,6,†] Andrew T. Lytle,[5,6] Craig McNeile,[13] Ethan T. Neil,[14] Curtis T. Peterson,[1] James N. Simone,[9] Jacob W. Sitison,[14,‡] Ruth S. Van de Water,[9] and Alejandro Vaquero[3,15,16]

(Fermilab Lattice, HPQCD, and MILC Collaborations)

[1] *Department of Computational Mathematics, Science and Engineering, and Department of Physics and Astronomy, Michigan State University, East Lansing, Michigan 48824, USA*
[2] *Department of Physics, Washington University, St. Louis, Missouri 63130, USA*
[3] *Department of Physics and Astronomy, University of Utah, Salt Lake City, Utah 84112, USA*
[4] *SUPA, School of Physics and Astronomy, University of Glasgow, Glasgow G12 8QQ, United Kingdom*
[5] *Department of Physics, University of Illinois Urbana-Champaign, Urbana, Illinois, 61801, USA*
[6] *Illinois Center for Advanced Studies of the Universe, University of Illinois Urbana-Champaign, Urbana, Illinois, 61801, USA*
[7] *CAFPE and Departamento de Física Teórica y del Cosmos, Universidad de Granada, E-18071 Granada, Spain*
[8] *Department of Physics, Indiana University, Bloomington, Indiana 47405, USA*
[9] *Theory Division, Fermi National Accelerator Laboratory, Batavia, Illinois, 60510, USA*
[10] *Department of Physics, Colorado State University, Fort Collins, Colorado 80523, USA*
[11] *Department of Physics, Syracuse University, Syracuse, New York 13244, USA*
[12] *Laboratory for Elementary-Particle Physics, Cornell University, Ithaca, New York 14853, USA*
[13] *Centre for Mathematical Sciences, University of Plymouth, Plymouth PL4 8AA, United Kingdom*
[14] *Department of Physics, University of Colorado, Boulder, Colorado 80309, USA*
[15] *Departmento de Física Teórica, Universidad de Zaragoza, 50009 Zaragoza, Spain*
[16] *Center for Astroparticles and High Energy Physics (CAPA), Calle Pedro Cerbuna 12, 50009 Zaragoza, Spain*

(Dated: December 25, 2024)

We present results for the dominant light-quark connected contribution to the long-distance window (LD) of the hadronic vacuum polarization contribution (HVP) to the muon $g-2$ from lattice quantum chromodynamics (QCD). Specifically, with a new determination of the lattice scale on MILC's physical-mass HISQ ensembles, using the Ω^- baryon mass, we obtain a result of $a_\mu^{ll,\,\mathrm{LD}}(\mathrm{conn.}) = 401.2(2.3)_{\mathrm{stat}}(3.6)_{\mathrm{syst}}[4.3]_{\mathrm{total}} \times 10^{-10}$. In addition, following up on our recent work on the short- (SD) and intermediate-distance (W) windows, we report updated values for these quantities with this new scale-setting determination. Summing these individual window contributions enables a sub-percent precision determination of the light-quark-connected contribution to HVP of $a_\mu^{ll}(\mathrm{conn.}) = 656.2(1.9)_{\mathrm{stat}}(4.0)_{\mathrm{syst}}[4.4]_{\mathrm{total}} \times 10^{-10}$. Finally, as a consistency check, we verify that an independent analysis of the full contribution is in agreement with the sum of individual windows. We discuss our future plans for improvements of our HVP calculations to meet the target precision of the Fermilab g-2 experiment.

INTRODUCTION

The muon's anomalous magnetic moment or "muon $(g-2)$" is one of the most sensitive probes of the Standard Model of particle physics, with both the experimental results [1, 2] and the Standard Model prediction [3] reaching precisions well below one part per million. Tensions between theory and experiment in this quantity have long captured the attention of particle physicists since the results of the E821 experiment at Brookhaven [4]. With forthcoming experimental results from Fermilab [2] and J-PARC [5, 6] expected to improve further the accuracy of the muon $(g-2)$ measurement, concurrent improvements in the Standard Model theoretical calculation are urgently needed.

Although they are a relatively small part of the total prediction, the contributions to the muon $(g-2)$ from hadronic physics are among the most challenging to calculate due to strong-coupling effects. The muon does not feel the strong force directly, so these contributions arise from corrections to either the photon two-point function (hadronic vacuum polarization, or HVP), or the photon four-point function (hadronic light-by-light scattering, or HLbL). As described in detail in Ref. [3], both HVP and HLbL can be estimated either from dispersive theory relying on experimental measurements of hadronic processes or calculated *ab initio* using lattice QCD.

Of these quantities, HLbL represents a smaller contribution to muon $(g-2)$ but is also more difficult to calculate precisely. While previous summary reports from the

Muon $g-2$ Theory Initiative [3, 7] already found good agreement between dispersive evaluations [8–21] and lattice QCD calculations [22, 23], more recent lattice and dispersive results [24–54] are rapidly pushing this quantity towards the precision goals needed for the final muon $(g-2)$ experimental results.

For HVP, rapid progress on the lattice QCD side [55–67] has revealed tensions between lattice HVP results and data-driven dispersive estimates [7, 68]. Efforts to understand these tensions, as well as to cross-check systematic effects in lattice calculations from different groups, have led to widespread study of HVP restricted to Euclidean windows [69], which isolate the contribution from a particular temporal range. Corresponding dispersive estimates of HVP restricted to the same windows [68, 70–73] can be studied and compared with lattice results, an approach that can help shed light on these tensions.

In this work, we present results for the dominant long-distance window (LD) contribution to HVP, specifically the connected contributions from light (up and down) quarks in the isospin-symmetric limit, which comprise about 90% of the total HVP. LD quantities suffer from large statistical noise and are sensitive to systematic effects from finite lattice volume and scale-setting [74] uncertainties. This work employs the high-statistics lattice datasets that were used to study the short- and intermediate-distance contributions in Ref. [67], a companion paper to this work. In addition, here we set the lattice scale at high precision using the mass of the Ω^- baryon [75, 76]. The combination of high statistics and improved scale setting allows us to achieve greatly improved precision for the LD HVP as well as for the full light-quark connected HVP by summing our LD result with the other window observables calculated in Ref. [67], and updated here with the improved scale setting.

DEFINITIONS

The leading-order hadronic-vacuum-polarization contribution to the muon anomalous magnetic moment $a_\mu \equiv (g-2)_\mu/2$ is obtained via

$$a_\mu^{\mathrm{HVP,LO}} = 4\alpha^2 \int_0^\infty \mathrm{d}t\, C(t)\tilde{K}(t), \tag{1}$$

where α is the fine-structure constant, the kernel $\tilde{K}$ stems from quantum electrodynamics (QED) [77, 78], and $C(t) = \frac{1}{3}\sum_{k=1}^{3}\sum_{\boldsymbol{x}}\left\langle J^k(\boldsymbol{x},t)J^k(0)\right\rangle$ is the Euclidean-time two-point correlation function of the electromagnetic current $J^\mu(x) = \sum_f q_f \bar{\psi}_f(x)\gamma^\mu\psi_f(x)$, which is summed over all quark flavors $f \in \{u,d,s,c,b,t\}$ of electric charge q_f. Lattice-QCD calculations of $a_\mu^{\mathrm{HVP,LO}}$ separately compute the contributions from each quark flavor and from connected and disconnected Wick contractions. Additionally, these calculations are performed in the isospin-symmetric limit in pure QCD with the effects of strong-isospin breaking and QED added as corrections; these correction terms have been studied in Ref. [67]. In this work, we focus on the dominant isospin-symmetric, light-quark connected (LQC) contribution $a_\mu^{ll}(\mathrm{conn.})$.

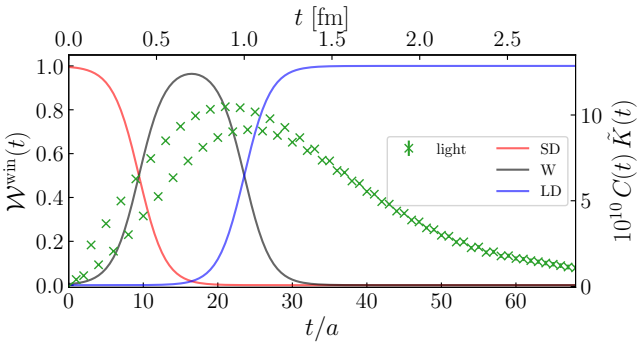

FIG. 1. The SD (red), W (black), and LD (blue) window functions as defined in the text, overlaid with raw lattice data for the LQC vector correlator convolved with the integration kernel $C(t)\tilde{K}(t)$ (green crosses) on our 0.06 fm ensemble.

In addition to the complete LQC $a_\mu^{ll}(\mathrm{conn.})$ defined by Eq. (1), which we refer to here as the "full" contribution, one may consider window observables [69] that restrict the Euclidean-time region over which $C(t)$ is integrated,

$$a_\mu^{\mathrm{win}} = 4\alpha^2 \int_0^\infty \mathrm{d}t\, C(t)\tilde{K}(t)\mathcal{W}^{\mathrm{win}}(t)\,. \tag{2}$$

While there are many ways to define such a window function, in this work we focus on the "long-distance" window defined by

$$\mathcal{W}^{\mathrm{LD}}(t) = \frac{1}{2}\left[1+\tanh\left(\frac{t-t_1}{\Delta}\right)\right], \tag{3}$$

with $t_1 = 1$ fm, and $\Delta = 0.15$ fm. This window is complemented by the "short-" and "intermediate-distance" windows, defined in Eqs. (2.9)–(2.12) of Ref. [67] and studied there in detail, to cover the full integration region. The functions for the three complementary windows (SD, W, and LD) are shown in Fig. 1. The LD window covers the tail of the integrand, also shown in Fig. 1, where statistical errors increase significantly. Our strategies for alleviating this issue are discussed in detail below and in the appendix.

PHYSICAL INPUTS

This calculation makes use of ensembles of four-flavor gauge-field configurations. Converting the lattice results into physical units requires the selection of a set of physical inputs that determine the quark masses and the lattice spacing (or scale). The masses of the u, d, s, and c quarks are determined by the masses of the π^+, K^0, K^+,

and D_s^+ mesons. In the "isospin-symmetric, pure-QCD world" that corresponds to work done here, where the up- and down-quark masses are taken to be equal and QED effects are removed, we define the physical point with $M_{\pi^+} = 134.977$ MeV, $M_K = 494.496$ MeV, and $M_{D_s} = 1967.02$ MeV. In this prescription, we work with the physical light-quark mass $m_l \equiv (m_u + m_d)/2$. We direct the reader to our previous work for more details [67].

We set the lattice scale using the Ω^- baryon mass [75, 76]. To fix the scale to the pure-QCD world, we use the value of $M_\Omega = 1.67126(32)$ GeV [75, 76], which has had the QED effects subtracted. We also consider a secondary scale setting based on the pion decay constant f_π [79–81] using the physical value $f_\pi = 0.13050(13)$ GeV [82], allowing a consistency check between the two most commonly used scale-setting observables for a_μ^{ll}(conn.). Values for aM_Ω and af_π on the ensembles used in this work are given in Table I.

LATTICE ENSEMBLES AND CORRELATION FUNCTIONS

The lattice ensembles and correlation function datasets employed in this work are described in detail in our companion paper, Ref. [67]. Briefly, this work employs gauge field ensembles generated by the MILC collaboration [83–85] with light, strange, and charm quarks in the sea (all tuned to their physical values) spanning the range of lattice spacings of $a \approx 0.15$–0.06 fm, as summarized in Table I.[1] Further details on the quark masses and corresponding meson masses are given in Table II of Ref. [67]. The vector-current two-point correlation function datasets are described in Table IV of Ref. [67] and the corresponding renormalization factors Z_V are taken from Refs. [87, 88] and listed in Table III of Ref. [67]. We use the "local" and "one-link" current datasets, which correspond to two different discretizations of the vector current, on the $a \approx 0.12, 0.09, 0.06$ fm ensembles, all of which were generated using low-mode averaging (LMA) [89–91]. In addition, our analysis includes new correlation function datasets generated on 957 configurations of the $a \approx 0.15$ fm ensemble using LMA with 1000 eigenvectors.

ANALYSIS STRATEGY

Our overall strategy for HVP observables is described in our companion paper, Ref. [67]. In particular, the blinding procedure, lattice corrections, continuum fit functions and strategy for performing the continuum extrapolations, the Bayesian Model Averaging (BMA), and systematic error estimates follow the detailed description of Ref. [67]. As in Ref. [67], each individual HVP observable was multiplied with an unknown blinding factor, which was removed only after the analysis was finalized.

Long-distance HVP observables are affected by the well-known, rapid growth of statistical errors in the vector-current correlation functions [92]. While the exact low-modes used in the generation of the correlators help to reduce the statistical errors at large Euclidean times, these errors are still a significant source of uncertainty. We address this issue with a correlator-reconstruction strategy to replace $C(t)$ at large times. In Ref. [93], a precise reconstruction of the vector-current correlator at large times, obtained from an exclusive channel study of the two-pion contributions, was used to test the fit method (described below). The fit was found to provide a reliable, albeit less precise, description of the vector-current correlator in the long time region. Hence, our results are obtained with this approach; we also employ the bounding method [69] as a cross-check (see appendix).

FIT METHOD

In this approach, the correlation-function data are fit over the range $t_{\rm min} \le t \le t_{\rm max}$ to a function matching the expected spectral decomposition. The noisy correlation function data is then replaced with the fit reconstruction at large Euclidean distances, $t \ge t^\star$, where $t^\star$ is a hyperparameter that we optimize by minimizing the overall variance of a_μ.

The spectral decompositions of the staggered correlation functions employed in this analysis contain two towers of states, one of which has an oscillating phase, yielding the following fit function:

$$C_{\rm fit}(t) = \text{const.} + \sum_{n=0}^{N_{\rm states}} \left[Z_n^2 \left(e^{-E_n t} + e^{-E_n (T-t)} \right) \right] + (-1)^t \sum_{m=0}^{M_{\rm states}} \left[Z_{m,\rm osc}^2 \left(e^{-E_{m,\rm osc} t} + e^{-E_{m,\rm osc}(T-t)} \right) \right], \tag{4}$$

where the energies $(E_n, E_{m,\rm osc})$, amplitudes $(Z_n, Z_{m,\rm osc})$, and constant term are the parameters obtained from the fit. Here, $T = aN_t$ is the temporal extent of the lattice, and the term that is constant in time separation t incorporates the leading additional finite-T effects [93, 94]. The vector-current correlators are too noisy to resolve precisely the low-lying two-pion states that contribute to the correlator at large times. Hence, the low-lying spectrum obtained with the fit method is only approximate, representing a mix of the ρ meson and two-pion states.

[1] The 0.09 fm ensemble was, in-part, generated by the CalLat collaboration [86] using retuned values of the quark masses determined by MILC [79].

TABLE I. Ensemble parameters used in this work. The first column lists the approximate lattice spacings in fm. The second column gives the spatial length L of the lattices in fm. The third column lists the volumes of the lattices in number of space-time points. The fourth column gives the sea-quark masses in lattice-spacing units. The fifth column lists the Ω^- baryon mass in lattice units, aM_Ω [75, 76]. The sixth column lists the values of af_π.

$\approx a$/fm	L/fm	$N_s^3 \times N_t$	$am_l^{\rm sea}/am_s^{\rm sea}/am_c^{\rm sea}$	aM_Ω	af_π
0.15	4.85	$32^3 \times 48$	0.002426/0.0673/0.8447	1.3246(26)	0.100269(44)
0.12	5.81	$48^3 \times 64$	0.001907/0.05252/0.6382	1.0494(17)	0.080330(62)
0.09	5.61	$64^3 \times 96$	0.001326/0.03636/0.4313	0.75372(97)	0.058177(63)
0.06	5.45	$96^3 \times 128$	0.0008/0.022/0.260	0.4834(11)	0.037553(32)

Rather than using a single fit Ansatz, we carry out a model average over multiple values of $t_{\rm min}$ using the Bayesian Akaike information criterion (BAIC) with the data-subset penalty [95, 96], holding $t_{\rm max}$ fixed at a value beyond which the noise-to-signal rises above 85%. The value of $t_{\rm min}$ is allowed to vary over a restricted range, as described in the appendix. Log-normal priors are employed for the energies and amplitudes, following Ref. [97]; the prior for the constant term is set based on the energy and amplitude priors to match the leading constant contribution of $Z_0^2 e^{-E_\pi T}$. Choices of fit hyperparameters and results for ground-state energies are given in the appendix.

Our final $C(t)$ which enters into Eqs. (1) and (2), in order to obtain a_μ on each ensemble, is obtained by taking the raw data $C(t)$ for $t < t^\star$ and $C_{\rm recon.}(t)$ for $t \geq t^\star$; the latter corresponds to the prediction of the fit model Eq. (4) evaluated in the limit $T \to \infty$. Other variations of the analysis choices, such as changing the number of states, have been tested and have negligible impact on the results.

Following the correlator reconstruction, to calculate a_μ, we extend the independent time range of our correlation function dataset from $N_t/2 + 1$ to $2N_t$ using the infinite-T correlator-reconstruction and then integrate Eqs. (1) and (2) using the trapezoidal rule. All error propagation is carried out using GVAR [98], cross-checked using jackknife resampling.

LATTICE CORRECTIONS

We perform explicit corrections for finite volume (FV), pion-mass (M_π) mistuning, and (optionally) taste breaking (TB) in that order, using the effective field theory (EFT) based correction schemes described in Ref. [67].

The finite spatial-volume and TB corrections used for the LQC contribution are shown in the appendix; M_π-mistuning corrections are small due to the accurate tuning of the ensemble masses and hence are not shown. We also include a finite-time correction using next-to-leading order chiral perturbation theory (NLO χPT) [55]; we find the size of this correction is sub-permille.

CONTINUUM EXTRAPOLATIONS

The continuum extrapolations of our $a_\mu^{ll,\,\rm LD}$(conn.) and a_μ^{ll}(conn.) data are based on the form $a_\mu(a, M_A) = a_\mu \left[1 + F^a(a) + F^M(M_A)\right]$ where $F^M(M_A)$ accounts for residual sea-quark-mass–mistuning effects and is given in Eq. (3.7) of Ref. [67] and

$$F^a(a) = C_{a^2,n}(a\Lambda)^2\alpha_s^n + \sum_{k=2}^{m} C_{a^{2k}}(a\Lambda)^{2k}, \qquad (5)$$

where $n = 1, 2$ ($n = 0$) for the local (one-link) current, and $m = 2, 3$. In joint fits to data obtained from the local and one-link currents, the parameters in $F^M(M_A)$ and a_μ are shared.

We first employ the empirical Bayes procedure discussed in Sec. III.C of Ref. [67] to obtain guidance for the choice of scale Λ and the relevant terms in the continuum fit function. The procedure is performed for both currents independently and jointly, and separately for data corrected and not corrected for TB effects. After varying the correction schemes and windows, as well as correlator-reconstruction methods, we find $\Lambda \approx 0.5$ GeV for data corrected for TB effects and $\Lambda \approx 1.0$ GeV for uncorrected data, reflecting the fact that discretization effects are larger in the uncorrected a_μ^{ll}(conn.) data. The empirical Bayes analysis further reveals that the data corrected for TB is sensitive to discretization terms up to a^4 whereas the uncorrected data is sensitive to terms up to a^6. Hence, we consider variations of the functions $F^a(a)$ where $m = 2$ (quadratic) or $m = 3$ (cubic). For the quadratic fits, we consider a variation where the 0.15 fm data point is dropped. For datasets not corrected for TB effects, we perform only joint fits and fix $n = 2$ for the local current, to account for the dominant TB effects [59].

CONTINUUM EXTRAPOLATION BMA

The systematic uncertainties associated with analysis or model choices are estimated using BMA [95, 99]. This procedure and relevant formulae are detailed in Refs. [59, 67]. In the BMA, we include variations for all FV, M_π-mistuning and TB correction schemes

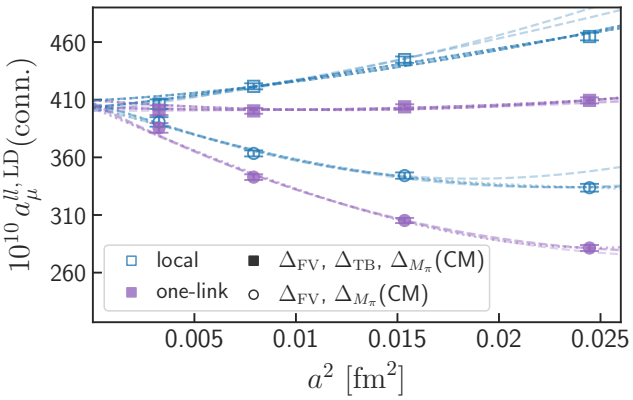

FIG. 2. Continuum extrapolations of the long-distance window observable $a_\mu^{ll,\,\mathrm{LD}}(\mathrm{conn.})$. Data points shown are corrected for FV and M_π mistuning using the CM scheme. Blue unfilled (purple filled) points are from the local (one-link) current. Squares (circles) represent data corrected (uncorrected) for TB using the CM scheme. Different extrapolations are obtained from variations of the fit functions and ensembles included.

TABLE II. Approximate absolute error budgets (in units of 10^{-10}) for the uncertainties reported in Eqs. (6)–(9). From left to right, the contributions to the error are Monte Carlo statistics and t_{min} variations in the correlator reconstructions for $a_\mu^{ll,\,\mathrm{LD}}$ and a_μ^{ll}, continuum extrapolation and TB corrections, FV and M_π-mistuning corrections, scale setting, and current renormalization.

Contrib.	stat., t_{min}	$a\to 0$, Δ_{TB}	Δ_{FV}, Δ_{M_π}	a	Z_V	Total
$a_\mu^{ll,\,\mathrm{SD}}$	0.009	0.056	—	0.024	0.062	0.087
$a_\mu^{ll,\,\mathrm{W}}$	0.14	0.38	0.32	0.31	0.17	0.62
$a_\mu^{ll,\,\mathrm{LD}}$	2.3	2.7	1.4	1.9	0.2	4.3
a_μ^{ll}	2.0	3.0	1.8	1.8	0.3	4.4

discussed in the appendix, namely NNLO χPT, chiral model (CM), and Meyer-Lellouch-Lüscher-Gounaris-Sakurai (MLLGS). We always correct both currents using the same scheme. Extrapolations using MLLGS exclude the coarsest data point (0.15 fm) as discussed in Ref. [67]. FV and M_π-mistuning corrections are always included, along with a 10% associated uncertainty to capture differences between EFT-based and data-driven corrections [55, 63, 65]. Variations with and without TB corrections are considered.

We perform continuum extrapolations using all fit function variations described above, including fits that exclude one of the two currents entirely [67]. Sample individual results from the continuum extrapolation BMA for $a_\mu^{ll,\,\mathrm{LD}}(\mathrm{conn.})$ are shown in Fig. 2. Additional results and details, including with the alternative f_π scale setting, are shown in the appendix.

RESULTS

Here we report our main results, which use M_Ω scale setting and the fit method for correlator reconstructions. Error budgets for all listed quantities below are given in Table II. Additional results for f_π scale setting or the bounding method are given in the appendix. First, we update our results for $a_\mu^{ll,\,\mathrm{SD}}(\mathrm{conn.})$ and $a_\mu^{ll,\,\mathrm{W}}(\mathrm{conn.})$ from Ref. [67].[2,3] We find

$$a_\mu^{ll,\,\mathrm{SD}}(\mathrm{conn.}) = 48.119(9)(87)[87]\times 10^{-10}, \quad (6)$$

$$a_\mu^{ll,\,\mathrm{W}}(\mathrm{conn.}) = 206.96(14)(60)[62]\times 10^{-10}, \quad (7)$$

where the uncertainties are statistical (second column of Table II), systematic (third to sixth columns of Table II) and total. These new determinations are, unsurprisingly, completely consistent with our previous results, given that the analysis is fixed. For the long-distance window we obtain,

$$a_\mu^{ll,\,\mathrm{LD}}(\mathrm{conn.}) = 401.2(2.3)(3.6)[4.3]\times 10^{-10}. \quad (8)$$

Summing the LQC contribution in the three windows, Eqs. (6)–(8), with the correlation matrix given in the appendix, yields

$$a_\mu^{ll}(\mathrm{conn.}) = 656.2(1.9)(4.0)[4.4]\times 10^{-10}. \quad (9)$$

Finally, from the independent analysis of the full integration region we obtain $a_\mu^{ll,\,\mathrm{Full}}(\mathrm{conn.}) = 655.2(2.4)(4.5)[5.1]\times 10^{-10}$, a result that is completely consistent with Eq. (9) with a correlated difference of $1.1(5.4)\times 10^{-10}$.

SUMMARY AND OUTLOOK

As part of our ongoing lattice QCD project to calculate the complete HVP with few-permille precision, we have calculated $a_\mu^{ll,\,\mathrm{LD}}(\mathrm{conn.})$ at 1.1% precision, while we obtain $a_\mu^{ll}(\mathrm{conn.})$ with a total uncertainty of 0.67%, the most precise determination of this important quantity from lattice QCD to date.[4] These results are made possible by the high-statistics correlation function data set we have generated to date [67], as well as the new high-precision scale-setting using the Ω^- baryon mass [75, 76].

A comparison of our results for $a_\mu^{ll,\,\mathrm{LD}}(\mathrm{conn.})$, using both M_Ω and f_π scale settings, with those of the

[2] The values of aM_Ω and af_π that we use on our ensemble with $a\approx 0.04$ fm are 0.3608(25) and 0.028099(28), respectively.

[3] Two corrupted configurations were removed from the 0.04 fm one-link dataset. Additionally, missing correlations in the one-link renormalization factors, arising from the fact the 0.04 value comes from a fit to the factors at coarser spacings, were included.

[4] Our results for $a_\mu^{ll,\,\mathrm{LD}}(\mathrm{conn.})$ and $a_\mu^{ll}(\mathrm{conn.})$ obtained from f_π scale setting are at 0.98% and 0.61% precision, respectively.

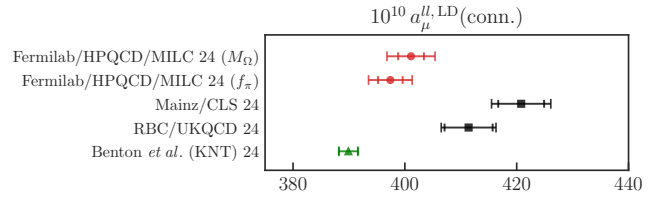

FIG. 3. Comparison of our lattice determinations for $a_\mu^{ll,\,\mathrm{LD}}$(conn.) (filled red circles) labeled "Fermilab/HPQCD/MILC 24" with $n_f = 2+1$ (black squares) lattice-QCD calculations by Mainz/CLS 24 [65], RBC/UKQCD 24 [63]. The inner error bar shown for our result is from Monte Carlo statistics. Also shown is a data-driven evaluation of $a_\mu^{ll,\,\mathrm{LD}}$(conn.) using e^+e^- cross section data (green triangle) by Benton *et al.* 24 [68].

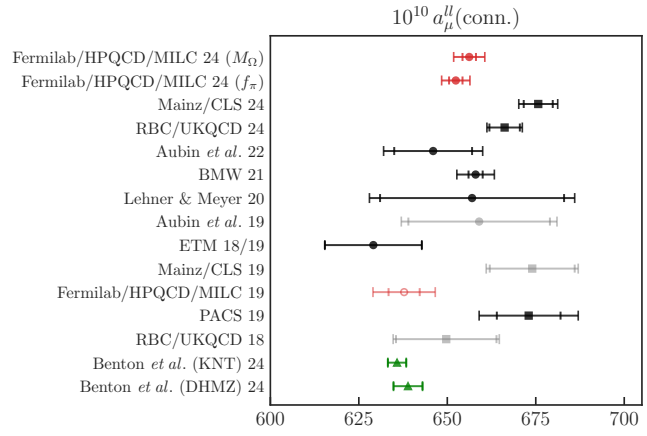

FIG. 4. Comparison of our lattice determinations for a_μ^{ll}(conn.) (filled red circles) labeled "Fermilab/HPQCD/MILC 24" with $n_f = 2+1+1$ (black circles) and $n_f = 2+1$ (black squares) lattice-QCD calculations by Mainz/CLS 24 [65], RBC/UKQCD 24 [63], Aubin *et al.* 22 [56], BMW 21 [55], Lehner & Meyer 20 [100], Aubin *et al.* 19 [101], ETM 18/19 [102], Mainz/CLS 19 [103], PACS 19 [104], and RBC/UKQCD 18 [69]. Our previous determination, Fermilab/HPQCD/MILC 19 [105], is shown with an unfilled red circle. Inner error bars indicate the reported statistical uncertainty. Also shown are data-driven evaluations of a_μ^{ll}(conn.) using e^+e^- cross section data (green triangles) by Benton *et al.* 24 [68].

RBC/UKQCD [63] and Mainz [65] collaborations as well as a data-driven evaluation [68] is shown in Fig. 3. Using the same scale setting in the comparisons with other lattice-QCD results, we find that our result is lower than RBC/UKQCD 24 (M_Ω) and Mainz 24 (f_π) by 1.6σ and 3.6σ, respectively, while being higher than the data-driven evaluation of Ref. [68] by 2.4σ, if using M_Ω. In Fig. 4 we compare our result for a_μ^{ll}(conn.) with previous lattice-QCD calculations as well as the data-driven evaluations of Ref. [68]. Focusing on the three most precise lattice-QCD results, we find significances of 0.3σ with BMW 21 (M_Ω), 1.5σ with RBC/UKQCD 24 (M_Ω), and 3.5σ with Mainz 24 (f_π). We find a difference of 1.5σ with our previous result of Ref. [97], if using the f_π scale. For a more direct comparison with Ref. [97] we take our result from the direct analysis of the full integration region obtained with f_π scale setting of $a_\mu^{ll,\mathrm{Full}}(\mathrm{conn.}) = 651.1(4.8) \times 10^{-10}$ (see the appendix), which yields a significance of 1.3σ. Finally, we find that our result in Eq. (9) differs from the data-driven evaluation of Ref. [68] by 4.0σ (2.9σ) if using the KNT (DHMZ) compilations, confirming the tensions between lattice-QCD and data-driven evaluations seen previously and in windowed HVP observables. More precise lattice-QCD calculations are clearly needed.

Looking towards future improvements of our HVP calculations, we are generating correlators on ensembles with both a finer lattice spacing $a \approx 0.04$ fm and with a larger spatial length $L \approx 11$ fm at $a \approx 0.09$ fm, both of which will help to address significant sources of uncertainty (as shown in Table II.) We also plan to add exclusive two-pion channel correlator data, which is expected to greatly improve the statistical precision for LD HVP, even for staggered fermions [93], as well as parallel improved calculations of subleading contributions due to quark-disconnected diagrams and isospin-breaking effects [67]. Taken all together, we expect that these improvements will allow us to meet the target precision set by the Fermilab $g-2$ experiment.

ACKNOWLEDGMENTS

We are grateful to Yin Lin, Aaron Meyer, and Michael Wagman for their contributions to the Ω^- scale-setting project, the results of which are used in this work. We thank Urs Heller for his contributions to our projects on gauge flow and the pion decay constant, also used in scale setting.

Computations for this work were carried out in part with computing and long-term storage resources provided by the USQCD Collaboration, the National Energy Research Scientific Computing Center (Edison, Cori, Perlmutter), the Argonne Leadership Computing Facility (Mira, Theta) under the INCITE program, and the Oak Ridge Leadership Computing Facility (Summit, Frontier) under the Innovative and Novel Computational Impact on Theory and Experiment (INCITE) and the ASCR Leadership Computing Challenge (ALCC) programs. The Argonne Leadership Computing Facility (ALCF), is supported by the U.S. Department of Energy (USDOE) under contract DE-AC02-06CH11357. The National Energy Research Scientific Computing Center (NERSC) is located at Lawrence Berkeley National Laboratory and operated under USDOE Contract No. DE-AC02-05CH11231. (Our awards are HEP-ERCAP0032813, HEP-ERCAP0031326, and possible predecessors.) The Oak Ridge Leadership Computing Facility (OLCF) at the Oak Ridge National Labo-

ratory is supported by the USDOE under Contract No. DE-AC05-00OR22725. ALCF, NERSC, and OLCF are all USDOE Office of Science User Facilities. This work used the Extreme Science and Engineering Discovery Environment (XSEDE) supercomputer Stampede 2 at the Texas Advanced Computing Center (TACC) through allocation TG-MCA93S002. The XSEDE program is supported by the National Science Foundation under grant number ACI-1548562. Computations on the Big Red II+, Big Red 3, and Big Red 200 supercomputers were supported in part by Lilly Endowment, Inc., through its support for the Indiana University Pervasive Technology Institute. The parallel file system employed by Big Red II+ was supported by the National Science Foundation under Grant No. CNS-0521433. This work utilized the RMACC Summit supercomputer, which is supported by the National Science Foundation (awards ACI-1532235 and ACI-1532236), the University of Colorado Boulder, and Colorado State University. The Summit supercomputer is a joint effort of the University of Colorado Boulder and Colorado State University. Some of the computations were done using the Blue Waters sustained-petascale computer, which was supported by the National Science Foundation (awards OCI-0725070 and ACI-1238993) and the state of Illinois. Blue Waters was a joint effort of the University of Illinois at Urbana-Champaign and its National Center for Supercomputing Applications.

This work was supported in part by the U.S. Department of Energy, Office of Science, under Awards No. DE-SC0010005 (E.T.N. and J.W.S.), No. DE-SC0010120 (S.G.), No. DE-SC0015655 (A.X.K., S.L., M.L., A.T.L.), the "High Energy Physics Computing Traineeship for Lattice Gauge Theory" No. DE-SC0024053 (J.W.S.), and the Funding Opportunity Announcement Scientific Discovery through Advanced Computing: High Energy Physics, LAB 22-2580 (D.A.C., C.T.P., L.H., M.L., S.L.); by the Exascale Computing Project (17-SC-20-SC), a collaborative effort of the U.S. Department of Energy Office of Science and the National Nuclear Security Administration (H.J.); by the National Science Foundation under Grants Nos. PHY20-13064 and PHY23-10571 (C.D., D.A.C., S.L., A.V.), PHY23-09946 (A.B.), and Grant No. 2139536 for Characteristic Science Applications for the Leadership Class Computing Facility (L.H., H.J.) by the Simons Foundation under their Simons Fellows in Theoretical Physics program (A.X.K.); by the Universities Research Association Visiting Scholarship awards 20-S-12 and 21-S-05 (S.L.); by MICIU/AEI/10.13039/501100011033 and FEDER (EU) under Grant PID2022-140440NB-C21 (E.G.); by Consejeria de Universidad, Investigación e Innovación and Gobierno de España and EU – NextGenerationEU, under Grant AST22 8.4 (E.G.); by AEI (Spain) under Grant No. RYC2020-030244-I / AEI / 10.13039/501100011033 (A.V.); and by U.K. Science and Technology Facilities Council under Grant ST/T000945/1 (C.T.H.D). A.X.K. and E.T.N. are grateful to the Pauli Center for Theoretical Studies and the ETH Zürich for support and hospitality. This document was prepared by the Fermilab Lattice, HPQCD, and MILC Collaborations using the resources of the Fermi National Accelerator Laboratory (Fermilab), a U.S. Department of Energy, Office of Science, HEP User Facility. Fermilab is managed by Fermi Research Alliance, LLC (FRA), acting under Contract No. DE-AC02-07CH11359.

* shaun.lahert@gmail.com
† ml11@illinois.edu
‡ jacob.sitison@colorado.edu

[1] B. Abi *et al.* (Muon g-2), Phys. Rev. Lett. **126**, 141801 (2021), arXiv:2104.03281 [hep-ex].
[2] D. P. Aguillard *et al.* (Muon g-2), Phys. Rev. Lett. **131**, 161802 (2023), arXiv:2308.06230 [hep-ex].
[3] T. Aoyama *et al.*, Phys. Rept. **887**, 1 (2020).
[4] G. W. Bennett *et al.* (Muon g-2), Phys. Rev. D **73**, 072003 (2006), arXiv:hep-ex/0602035.
[5] M. Abe *et al.*, PTEP **2019**, 053C02 (2019).
[6] J-PARC muon $g-2$/EDM experiment, `https://g-2.kek.jp/`.
[7] G. Colangelo *et al.*, arXiv:2203.15810 [hep-ph] (2022).
[8] K. Melnikov and A. Vainshtein, Phys. Rev. **D70**, 113006 (2004).
[9] P. Masjuan and P. Sánchez-Puertas, Phys. Rev. **D95**, 054026 (2017).
[10] G. Colangelo, M. Hoferichter, M. Procura, and P. Stoffer, JHEP **04** (2017), 161.
[11] M. Hoferichter, B.-L. Hoid, B. Kubis, S. Leupold, and S. P. Schneider, JHEP **10** (2018), 141.
[12] A. Gérardin, H. B. Meyer, and A. Nyffeler, Phys. Rev. **D100**, 034520 (2019).
[13] J. Bijnens, N. Hermansson-Truedsson, and A. Rodríguez-Sánchez, Phys. Lett. **B798**, 134994 (2019).
[14] G. Colangelo, F. Hagelstein, M. Hoferichter, L. Laub, and P. Stoffer, JHEP **03** (2020), 101.
[15] V. Pauk and M. Vanderhaeghen, Eur. Phys. J. **C74**, 3008 (2014), arXiv:1401.0832 [hep-ph].
[16] I. Danilkin and M. Vanderhaeghen, Phys. Rev. **D95**, 014019 (2017), arXiv:1611.04646 [hep-ph].
[17] F. Jegerlehner, *The Anomalous Magnetic Moment of the Muon*, Vol. 274 (Springer, Cham, 2017).
[18] M. Knecht, S. Narison, A. Rabemananjara, and D. Rabetiarivony, Phys. Lett. **B787**, 111 (2018), arXiv:1808.03848 [hep-ph].
[19] G. Eichmann, C. S. Fischer, and R. Williams, Phys. Rev. **D101**, 054015 (2020), arXiv:1910.06795 [hep-ph].
[20] P. Roig and P. Sánchez-Puertas, Phys. Rev. **D101**, 074019 (2020), arXiv:1910.02881 [hep-ph].
[21] J. Leutgeb, J. Mager, and A. Rebhan, Phys. Rev. D **107**, 054021 (2023), arXiv:2211.16562 [hep-ph].
[22] T. Blum, N. Christ, M. Hayakawa, T. Izubuchi, L. Jin, C. Jung, and C. Lehner (RBC), Phys. Rev. Lett. **124**, 132002 (2020).
[23] E.-H. Chao, R. J. Hudspith, A. Gérardin, J. R. Green,

H. B. Meyer, and K. Ottnad, Eur. Phys. J. C **81**, 651 (2021), arXiv:2104.02632 [hep-lat].
[24] J. Bijnens, N. Hermansson-Truedsson, L. Laub, and A. Rodríguez-Sánchez, JHEP **10**, 203, arXiv:2008.13487 [hep-ph].
[25] J. Lüdtke and M. Procura, Eur. Phys. J. C **80**, 1108 (2020), arXiv:2006.00007 [hep-ph].
[26] J. Bijnens, N. Hermansson-Truedsson, L. Laub, and A. Rodríguez-Sánchez, JHEP **04**, 240, arXiv:2101.09169 [hep-ph].
[27] M. Hoferichter and P. Stoffer, JHEP **05**, 159, arXiv:2004.06127 [hep-ph].
[28] J. Leutgeb and A. Rebhan, Phys. Rev. D **104**, 094017 (2021), arXiv:2108.12345 [hep-ph].
[29] M. Zanke, M. Hoferichter, and B. Kubis, JHEP **07**, 106, arXiv:2103.09829 [hep-ph].
[30] I. Danilkin, M. Hoferichter, and P. Stoffer, Phys. Lett. B **820**, 136502 (2021), arXiv:2105.01666 [hep-ph].
[31] G. Colangelo, F. Hagelstein, M. Hoferichter, L. Laub, and P. Stoffer, Eur. Phys. J. C **81**, 702 (2021), arXiv:2106.13222 [hep-ph].
[32] L. Cappiello, O. Catà, and G. D'Ambrosio, Phys. Rev. D **105**, 056020 (2022), arXiv:2110.05962 [hep-ph].
[33] J. Bijnens, N. Hermansson-Truedsson, and A. Rodríguez-Sánchez, JHEP **02**, 167, arXiv:2211.17183 [hep-ph].
[34] M. Hoferichter, B. Kubis, and M. Zanke, JHEP **08**, 209, arXiv:2307.14413 [hep-ph].
[35] J. Lüdtke, M. Procura, and P. Stoffer, JHEP **04**, 125, arXiv:2302.12264 [hep-ph].
[36] P. Colangelo, F. Giannuzzi, and S. Nicotri, Phys. Lett. B **840**, 137878 (2023), arXiv:2301.06456 [hep-ph].
[37] M. Hoferichter, P. Stoffer, and M. Zillinger, JHEP **04**, 092, arXiv:2402.14060 [hep-ph].
[38] M. Hoferichter, P. Stoffer, and M. Zillinger, arXiv:2412.00190 [hep-ph] (2024).
[39] M. Hoferichter, P. Stoffer, and M. Zillinger, arXiv:2412.00178 [hep-ph] (2024).
[40] J. Bijnens, N. Hermansson-Truedsson, and A. Rodríguez-Sánchez, arXiv:2411.09578 [hep-ph] (2024).
[41] S. Holz, C. Hanhart, M. Hoferichter, and B. Kubis, Eur. Phys. J. C **82**, 434 (2022), [Addendum: Eur.Phys.J.C 82, 1159 (2022)], arXiv:2202.05846 [hep-ph].
[42] S. Holz, M. Hoferichter, B.-L. Hoid, and B. Kubis, arXiv:2411.08098 [hep-ph] (2024).
[43] J. Leutgeb, J. Mager, and A. Rebhan, arXiv:2411.10432 [hep-ph] (2024).
[44] P. Colangelo, F. Giannuzzi, and S. Nicotri, Phys. Rev. D **109**, 094036 (2024), arXiv:2402.07579 [hep-ph].
[45] E. J. Estrada, J. M. Márquez, D. Portillo-Sánchez, and P. Roig, arXiv:2411.07115 [hep-ph] (2024).
[46] A. S. Miramontes, K. Raya, A. Bashir, P. Roig, and G. Paredes-Torres, arXiv:2411.02218 [hep-ph] (2024).
[47] E. J. Estrada, S. Gonzàlez-Solís, A. Guevara, and P. Roig, arXiv:2409.10503 [hep-ph] (2024).
[48] N. Asmussen, E.-H. Chao, A. Gérardin, J. R. Green, R. J. Hudspith, H. B. Meyer, and A. Nyffeler, JHEP **04**, 040, arXiv:2210.12263 [hep-lat].
[49] E.-H. Chao, R. J. Hudspith, A. Gérardin, J. R. Green, and H. B. Meyer, Eur. Phys. J. C **82**, 664 (2022), arXiv:2204.08844 [hep-lat].
[50] T. Blum, N. Christ, M. Hayakawa, T. Izubuchi, L. Jin, C. Jung, C. Lehner, and C. Tu, arXiv:2304.04423 [hep-lat] (2023).
[51] A. Gérardin, W. E. A. Verplanke, G. Wang, Z. Fodor, J. N. Guenther, L. Lellouch, K. K. Szabo, and L. Varnhorst, arXiv:2305.04570 [hep-lat] (2023).
[52] C. Alexandrou *et al.* (Extended Twisted Mass), Phys. Rev. D **108**, 094514 (2023), arXiv:2308.12458 [hep-lat].
[53] T. Lin, M. Bruno, X. Feng, L.-C. Jin, C. Lehner, C. Liu, and Q.-Y. Luo, arXiv:2411.06349 [hep-lat] (2024).
[54] Z. Fodor, A. Gerardin, L. Lellouch, K. K. Szabo, B. C. Toth, and C. Zimmermann, arXiv:2411.11719 [hep-lat] (2024).
[55] S. Borsanyi *et al.* (BMW), Nature **593**, 51 (2021).
[56] C. Aubin, T. Blum, M. Golterman, and S. Peris, Phys. Rev. D **106**, 054503 (2022).
[57] C. Alexandrou *et al.* (Extended Twisted Mass), Phys. Rev. D **107**, 074506 (2023), arXiv:2206.15084 [hep-lat].
[58] M. Cè *et al.*, Phys. Rev. D **106**, 114502 (2022).
[59] A. Bazavov *et al.* (Fermilab Lattice, HPQCD, MILC), Phys. Rev. D **107**, 114514 (2023), arXiv:2301.08274 [hep-lat].
[60] T. Blum *et al.* (RBC, UKQCD), Phys. Rev. D **108**, 054507 (2023), arXiv:2301.08696 [hep-lat].
[61] A. Boccaletti *et al.*, (2024), arXiv:2407.10913 [hep-lat].
[62] S. Kuberski, M. Cè, G. von Hippel, H. B. Meyer, K. Ottnad, A. Risch, and H. Wittig, JHEP **03**, 172, arXiv:2401.11895 [hep-lat].
[63] T. Blum *et al.* (RBC, UKQCD), arXiv:2410.20590 [hep-lat] (2024).
[64] S. Spiegel and C. Lehner, arXiv:2410.17053 [hep-lat] (2024).
[65] D. Djukanovic, G. von Hippel, S. Kuberski, H. B. Meyer, N. Miller, K. Ottnad, J. Parrino, A. Risch, and H. Wittig, arXiv:2411.07969 [hep-lat] (2024).
[66] C. Alexandrou *et al.* (Extended Twisted Mass Collaboration (ETMC)), arXiv:2411.08852 [hep-lat] (2024).
[67] A. Bazavov *et al.* (Fermilab Lattice, HPQCD, MILC), arXiv:2411.09656 [hep-lat] (2024).
[68] G. Benton, D. Boito, M. Golterman, A. Keshavarzi, K. Maltman, and S. Peris, arXiv:2411.06637 [hep-ph] (2024).
[69] T. Blum *et al.* (RBC, UKQCD), Phys. Rev. Lett. **121**, 022003 (2018).
[70] G. Colangelo, A. X. El-Khadra, M. Hoferichter, A. Keshavarzi, C. Lehner, P. Stoffer, and T. Teubner, Phys. Lett. B **833**, 137313 (2022).
[71] G. Benton, D. Boito, M. Golterman, A. Keshavarzi, K. Maltman, and S. Peris, Phys. Rev. Lett. **131**, 251803 (2023), arXiv:2306.16808 [hep-ph].
[72] M. Davier, Z. Fodor, A. Gerardin, L. Lellouch, B. Malaescu, F. M. Stokes, K. K. Szabo, B. C. Toth, L. Varnhorst, and Z. Zhang, Phys. Rev. D **109**, 076019 (2024), arXiv:2308.04221 [hep-ph].
[73] G. Benton, D. Boito, M. Golterman, A. Keshavarzi, K. Maltman, and S. Peris, Phys. Rev. D **109**, 036010 (2024), arXiv:2311.09523 [hep-ph].
[74] M. Della Morte, A. Francis, V. Gülpers, G. Herdoíza, G. von Hippel, H. Horch, B. Jäger, H. B. Meyer, A. Nyffeler, and H. Wittig, JHEP **10** (2017), 020.
[75] A. Bazavov *et al.*, PoS **LATTICE2023**, 292 (2024), arXiv:2401.06522 [hep-lat].
[76] A. Bazavov *et al.* (Fermilab Lattice, MILC) (2025), in preparation.
[77] T. Blum, Phys. Rev. Lett. **91**, 052001 (2003), arXiv:hep-lat/0212018.

[78] D. Bernecker and H. B. Meyer, Eur. Phys. J. A **47**, 148 (2011).
[79] A. Bazavov *et al.* (Fermilab Lattice, MILC), Phys. Rev. D **90**, 074509 (2014).
[80] B. Chakraborty *et al.* (Fermilab Lattice, HPQCD, MILC), Phys. Rev. Lett. **120**, 152001 (2018).
[81] A. Bazavov, C. Bernard, *et al.* (Fermilab Lattice, MILC) (2025), in preparation.
[82] R. L. Workman *et al.* (Particle Data Group), PTEP **2022**, 083C01 (2022).
[83] A. Bazavov *et al.* (MILC), Phys. Rev. D **82**, 074501 (2010).
[84] A. Bazavov *et al.* (MILC), Phys. Rev. D **87**, 054505 (2013).
[85] A. Bazavov *et al.* (Fermilab Lattice, MILC), Phys. Rev. D **98**, 074512 (2018).
[86] N. Miller *et al.*, Phys. Rev. D **103**, 054511 (2021), arXiv:2011.12166 [hep-lat].
[87] D. Hatton, C. T. H. Davies, G. P. Lepage, and A. T. Lytle (HPQCD), Phys. Rev. D **100**, 114513 (2019), arXiv:1909.00756 [hep-lat].
[88] D. Hatton, C. T. H. Davies, B. Galloway, J. Koponen, G. P. Lepage, and A. T. Lytle (HPQCD), Phys. Rev. D **102**, 054511 (2020).
[89] T. A. DeGrand and S. Schaefer, Comput. Phys. Commun. **159**, 185 (2004).
[90] L. Giusti, P. Hernandez, M. Laine, P. Weisz, and H. Wittig, JHEP **04** (2004), 013.
[91] T. Blum, T. Izubuchi, and E. Shintani, Phys. Rev. D **88**, 094503 (2013), arXiv:1208.4349 [hep-lat].
[92] G. P. Lepage, in *Theoretical Advanced Study Institute in Elementary Particle Physics* (1989).
[93] S. Lahert, C. DeTar, A. X. El-Khadra, S. Gottlieb, A. S. Kronfeld, and R. S. Van de Water, arXiv:2409.00756 [hep-lat] (2024).
[94] B. Chakraborty, C. T. H. Davies, P. G. de Oliviera, J. Koponen, G. P. Lepage, and R. S. Van de Water (HPQCD), Phys. Rev. D **96**, 034516 (2017).
[95] E. T. Neil and J. W. Sitison, arXiv:2208.14983 [stat.ME] (2022).
[96] E. T. Neil and J. W. Sitison, Phys. Rev. E **108**, 045308 (2023), arXiv:2305.19417 [stat.ME].
[97] C. T. H. Davies *et al.* (Fermilab Lattice, HPQCD, MILC), Phys. Rev. D **101**, 034512 (2020).
[98] G. Lepage, C. Gohlke, and D. Hackett, `gplepage/gvar v11.10` (2022).
[99] W. I. Jay and E. T. Neil, Phys. Rev. D **103**, 114502 (2021).
[100] C. Lehner and A. S. Meyer, Phys. Rev. D **101**, 074515 (2020).
[101] C. Aubin, T. Blum, C. Tu, M. Golterman, C. Jung, and S. Peris, Phys. Rev. D **101**, 014503 (2020), arXiv:1905.09307 [hep-lat].
[102] D. Giusti, F. Sanfilippo, and S. Simula, Phys. Rev. D **98**, 114504 (2018), arXiv:1808.00887 [hep-lat].
[103] A. Gérardin, M. Cè, G. von Hippel, B. Hörz, H. B. Meyer, D. Mohler, K. Ottnad, J. Wilhelm, and H. Wittig, Phys. Rev. D **100**, 014510 (2019), arXiv:1904.03120 [hep-lat].
[104] E. Shintani and Y. Kuramashi (PACS), Phys. Rev. D **100**, 034517 (2019), arXiv:1902.00885 [hep-lat].
[105] C. E. DeTar *et al.* (Fermilab Lattice, HPQCD, MILC), PoS **LATTICE2019**, 070 (2019).
[106] S. Borsanyi *et al.* (Budapest-Marseille-Wuppertal), Phys. Rev. Lett. **121**, 022002 (2018), arXiv:1711.04980 [hep-lat].
[107] G. P. Lepage *et al.*, Nucl. Phys. B Proc. Suppl. **106**, 12 (2002).
[108] C. M. Bouchard, G. P. Lepage, C. Monahan, H. Na, and J. Shigemitsu, Phys. Rev. D **90**, 054506 (2014), arXiv:1406.2279 [hep-lat].
[109] G. Wang, T. Draper, K.-F. Liu, and Y.-B. Yang (χQCD), arXiv:2204.01280 [hep-lat] (2022).
[110] A. Bazavov *et al.* (Fermilab Lattice, MILC), Phys. Rev. D **93**, 113016 (2016).

Appendix A: Additional fit method results

Figure 5 shows individual fit results for the ground state parameters as a function of $t_{\rm min}/a$, compared with the corresponding BMA results. The allowed range of $t_{\rm min}$ is $[t_{\rm min:min}, t_{\rm min:max}]$, where $t_{\rm min:min}$ is selected as the first timeslice in the plateau in the ground-state fit parameters versus $t_{\rm min}$ starting near 1.35 fm for all ensembles and currents, and $t_{\rm min:max}$ is obtained by requiring that at least 9 data points are present to ensure that there are enough degrees of freedom to determine all fit parameters. Choices of fit hyperparameters and results for ground-state energies are tabulated in Table III. Note the convergence of $E_{0,\rm fit}$ between the two different currents seen as $a \to 0$, reflecting the vanishing of TB effects as the continuum limit is approached.

Appendix B: Bounding method

As an alternative to fitting the data, one can use an *Ansatz* for replacing data in the region where a single exponential dominates the spectral decomposition Eq. (4). This enables bounds to be imposed on $C(t)$ from observing that the true ground state in $C(t)$ is an interacting two-pion state with vector quantum numbers, which has lower energy than the mass of the ρ meson. A lower bound on this energy (and thus an *upper* bound on the exponentially decaying $C(t)$) comes from $E_{\pi\pi,\rm free} = 2\sqrt{(2\pi/L)^2 + M_\pi^2}$, the energy of two P-wave non-interacting pions in a finite volume.[5] An upper bound on the true ground-state energy (giving a *lower* bound on $C(t)$) is provided by the ground-state energy $E_{0,\rm fit}$ taken from the fitting method and corresponding BMA over $t_{\rm min}$. The bounding functions are defined from the correlator data point $C(t_c)$ by the relations

$$C_{\rm lower}(t) e^{-E_{0,\rm fit} t_c} = C(t_c) e^{-E_{0,\rm fit} t}, \qquad (10)$$

[5] In principle, one should instead use the interacting energy; however, the approximate use of the free energy here is well within the current precision of a_μ^{ll}(conn.). See Refs. [93, 106] for further discussion.

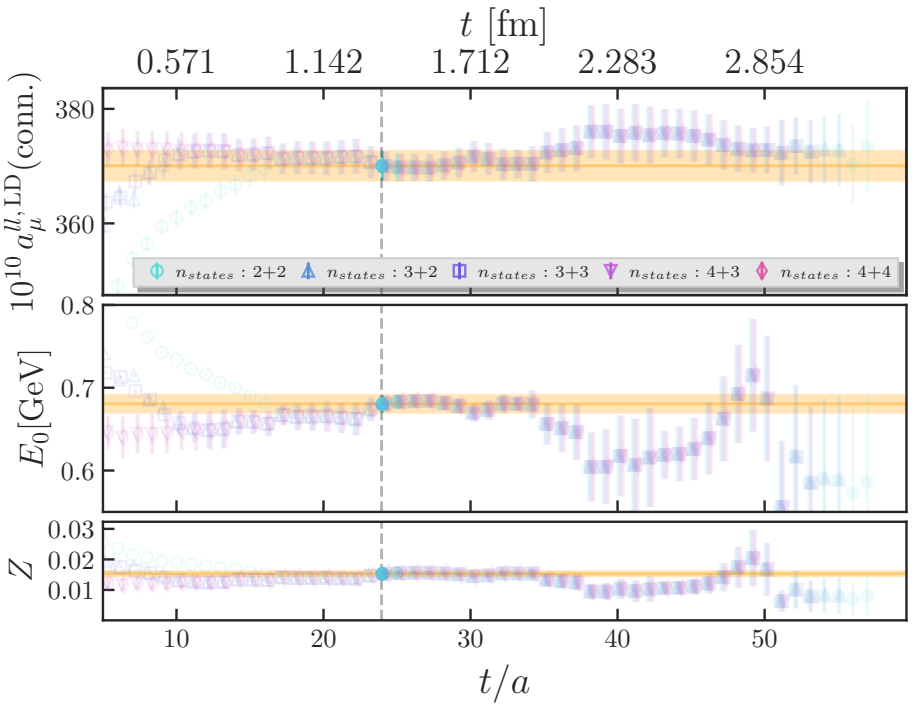

FIG. 5. Fit stability of a_μ (top panel), the ground state energy (middle panel) and amplitude (bottom panel) on the 0.06 fm ensemble using the local vector current operator. We perform a BMA over the set of points corresponding to $2+2$ states for all t_{min} after the dashed line. After the dashed line, the opacity of the points are proportional to their model weight in the BMA. The BMA result is given by the yellow band.

TABLE III. Description of operator measurements, hyperparameters, and ground-state energies used in the two correlator-reconstruction approaches employed in this work. The range of data points used to compute the bounding method result is from t_c to t_{max}.

$\approx a$/fm	J op.	# configs	t_{min}/fm range	t_{max}/fm	$t^\star$/fm	$E_{0,\mathrm{fit}}$/GeV	t_c/fm
0.15	local	957	[1.1, 1.6]	3.0	2.5	0.712(11)	2.8
	one-link	957	[0.9, 1.7]	3.1	2.0	0.7498(84)	2.7
0.12	local	1060	[1.4, 2.2]	3.4	3.2	0.685(26)	3.2
	one-link	1060	[1.2, 2.2]	3.4	2.7	0.715(12)	3.0
0.09	local	993	[1.3, 2.7]	3.5	2.8	0.692(13)	3.2
	one-link	993	[1.3, 2.6]	3.4	2.8	0.704(12)	3.1
0.06	local	1009	[1.4, 3.2]	3.7	2.5	0.681(11)	3.1
	one-link	900	[1.4, 3.1]	3.6	2.6	0.682(11)	3.1

$$C_{\mathrm{upper}}(t)C^0_{\pi\pi}(t_c,T) = C(t_c)e^{-E_{\pi\pi}t}, \tag{11}$$

where, for the upper bound, $C^0_{\pi\pi}(t_c,T) \equiv e^{-E_{\pi\pi}t_c} + e^{-E_{\pi\pi}(T-t_c)} + 2e^{-E_{\pi\pi}T/2}$ includes the leading corrections from the finite temporal extent T.

For both bounds, a time value t_c is selected such that the data are replaced with the bound for $t \geq t_c$. The value of t_c is determined for each $C(t)$ as the point where the upper and lower bounds meet, which we define as the time t_c where the absolute differences between upper and lower bound values at t_c/a and $t_c/a+1$ are less than the standard deviation of the correlated average $(C_{\mathrm{upper}} + C_{\mathrm{lower}})/2$ at each of the two points. The resulting t_c values are tabulated in Table III.

Once t_c is determined, the bound is used to replace the data for $t \geq t_c$. To mitigate the effect of statistical fluctuations, this replacement is done by averaging over the (even) range of points from t_c to t_{max}, inclusively, where t_{max} is the same as the value used in the fitting method above; if the number of time slices in this range is odd, the value of t_c/a is increased by 1. In addition, a systematic error is added equal to the difference in central values from repeating this procedure on the left and right (even, *i.e*, possibly overlapping) halves of the full range from t_c to t_{max} [106]. An example of the results from this procedure for the local current on the 0.06 fm ensemble is shown in Fig. 6 (left).

We compare the results of the two correlator-reconstruction approaches in Fig. 7. We find close agreement between the two approaches in most cases. How-

ever, on our finest ensemble ($a \approx 0.06$ fm), we observe that the bounding method approach does not handle significant correlated fluctuations in late time slices, which result in the tail of the correlator exhibiting non-exponential behavior, as can be seen in Fig. 6 (right), whereas the fit takes these correlations into account. Due to this difference, we adopt the fit method as our main result instead of attempting to average or combine it with the bounding method.

Appendix C: Lattice correction results

Results for FV and TB corrections are shown in Fig. 8. We consider three sub-windows of Eq. (3) from which we compute the corrections, where the boundaries are given by $t_1 = 0.4, 1, 1.5$ fm. These choices of t_1 are motivated by boundaries of the W, W2 and LD windows and the regions of validity of the various EFT-based correction schemes [56]. For a more detailed discussion of this approach see Sec. X and Sec. III.C of Refs. [56, 59]. Figure 8 shows that the expected dependencies on the lattice spacing, lattice volume, pion mass, and correction region are largely followed.

Appendix D: Details of BMA scheme

We use BMA to estimate systematic uncertainties associated with the various analysis choices that are included. We perform model averages at two stages in the analysis: over t_{min} variations to obtain correlator reconstructions, and then over the continuum extrapolation and lattice correction models. The mean and covariance from the BMA are given by

$$\langle A \rangle = \sum_{n=1}^{N_M} \langle A \rangle_n \, \text{pr}\left(M_n \mid D\right), \tag{12}$$

$$\begin{aligned} \text{Cov}[A,B] = &\sum_{n=1}^{N_M} \text{Cov}_n[A,B] \, \text{pr}\left(M_n \mid D\right) \\ &+ \sum_{n=1}^{N_M} \langle A \rangle_n \langle B \rangle_n \, \text{pr}\left(M_n \mid D\right) - \langle A \rangle \langle B \rangle , \end{aligned} \tag{13}$$

where A and B are each functions of the parameters of each model M_n, N_M is the number of models, and the probability of model M given the data D is defined through the BAIC weight [95],

$$\text{pr}(M \mid D) \equiv \text{pr}(M) \exp\left[-\frac{1}{2}\left(\chi^2_{\text{data}}\left(\mathbf{a}^\star\right) + 2k + 2N_{\text{cut}}\right)\right]. \tag{14}$$

χ^2_{data} is the standard chi-squared function not including the priors, $\mathbf{a}^\star$ is the posterior mode (*i.e.*, the set of parameters that minimizes the augmented chi-squared function [107]), k is the number of parameters in each model M, and N_{cut} is the number of data points cut from the dataset (t_{min} for correlator fits and the number of omitted ensembles for each current for continuum extrapolations). The factor $\text{pr}(M)$ is the prior probability of a given M, which we take to be uniform for correlator fits and as in Ref. [67] for continuum extrapolations.

The probability weights defined in Eq. (14) can be used to assess the relative weight of specific analysis choices in the BMA. Comparison of these weights can identify whether a particular correction scheme or fit-function variation is preferred or suppressed by the averaging procedure. This is achieved by computing the "subset probability" of the model subset S by the relative posterior probability of the variations contained in S:

$$\text{pr}(S|D) = \sum_{M_i \in S} \text{pr}(M_i|D). \tag{15}$$

The subset probability encapsulates the relative weight of the models in a given subset compared with the whole model space as informed by the data (see, *e.g.*, the pie charts in Fig. 11).

The first line of Eq. (13) gives the statistical and parametric contributions to the covariance, and the second line gives the systematic contribution from the spread of the different model variations in the average; we refer to the latter as "systematic covariance" here. In principle, the exact treatment of the systematic covariance requires including every combination of analysis choices through every stage of the analysis, *e.g.*, every t_{min} variation for every lattice spacing and current and every continuum extrapolation model. The number of such combinations is computationally infeasible. For the present analysis, we neglect the systematic covariances between the correlator fits on each lattice spacing and current; this assumption is equivalent to assuming the choice of t_{min} is independent between each lattice spacing and current. We also neglect this systematic covariance between the choices of t_{min} and the different continuum extrapolation models. These reasonable assumptions allow us to perform independent model averages and compose their results in series. For emphasis, the systematic contributions to the variances after each model average are not neglected, merely the systematic covariance between separate model averages.

In order to propagate statistical and parametric correlations though the series of model averages, it is useful to consider Eq. (13) in the case where one of the arguments is constant across the model space, *e.g.*, $\langle B \rangle_n = \langle B \rangle$. This will be true for scale-setting parameters, current renormalization factors, raw correlator data, and the results of other systematically independent model averages.

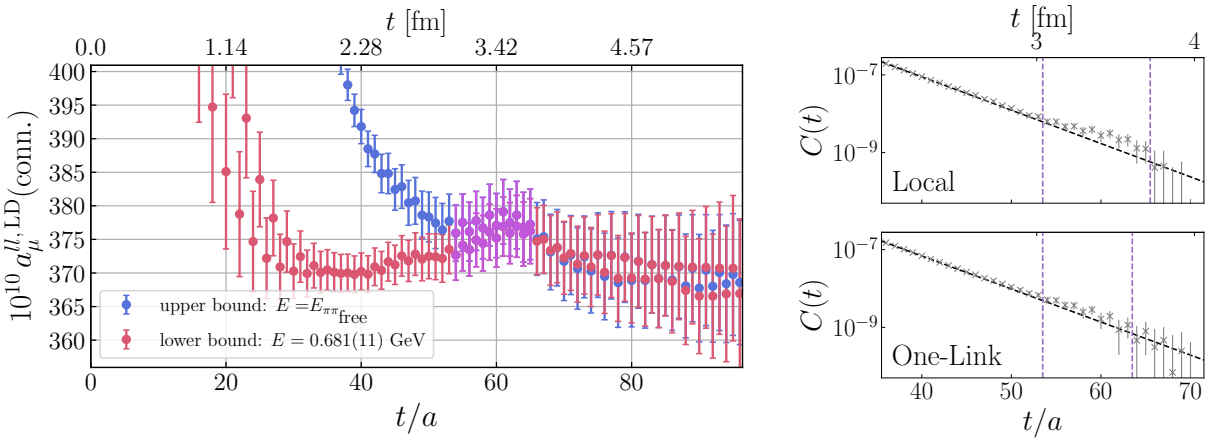

FIG. 6. *Left plot:* The bounding method applied to local vector current on the 0.06 fm ensemble. The range of data that are averaged to obtain the resultant a_μ is given in purple. *Right plot:* Correlator data (gray crosses) for local (upper panel) and one-link (lower panel) vector currents on the 0.06 fm ensemble. The vertical purple lines correspond to the ranges of $[t_c, t_{\mathrm{max}}]$ for each current. The black curve demonstrates the behavior of a one-state exponential decay fit to $C(t)$ at $t/a = 36$ and $t/a = 38$; deviations of $C(t)$ from the black curve illustrate where the correlator exhibits non-exponential behavior.

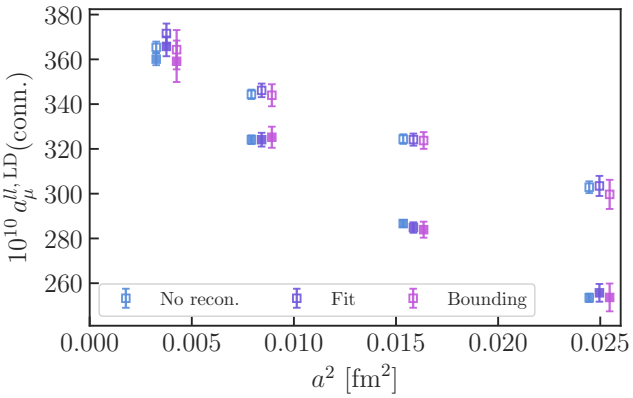

FIG. 7. Comparison of $a_\mu^{ll,\,\mathrm{LD}}(\mathrm{conn.})$ obtained from the two correlator-reconstruction approaches, the fit method (purple) and the bounding method (magenta), for the ensembles and currents used in this work. Also included is the result of using no correlator-reconstruction strategy ("No recon.," blue). The unfilled symbols correspond to the local current and the filled to the one-link.

In the example above, it follows that

$$\mathrm{Cov}[A, \overline{B}] = \sum_{n=1}^{N_M} \mathrm{Cov}_n[A, \overline{B}]\, \mathrm{pr}\,(M_n \mid D)\,, \tag{16}$$

where the bar denotes the parameter that is constant over the models M_n.

The above outlines the procedure used to obtain statistical and parametric covariances for continuum values of $a_\mu^{ll}(\mathrm{conn.})$ on each window. We also conservatively account for systematic correlations due to the shared use of lattice correction models on each window following the procedure in Ref. [67]. Additional systematic correlations due to common continuum model variations between windows, which were not relevant in Ref. [67], were considered and found to be negligible. These correlations will be reconsidered in future works when determining other full HVP observables beyond the LQC contribution.

Our procedure for obtaining complete error budgets from the respective BMA analyses is described in Refs. [59, 67]. In particular, we decompose the final uncertainty into its various contributions as described in Appendix A of Ref. [108]; the statistical and parametric contributions are computed approximately by using the best correlator fit, as determined by the BAIC, at each lattice spacing and current.

Appendix E: Additional results

Here we collect additional results for the various scale-setting schemes and correlator-reconstruction strategies considered. The final results for these variations are listed in Table IV. Updated comparison plots for $a_\mu^{ll,\,\mathrm{SD}}(\mathrm{conn.})$ and $a_\mu^{ll,\,\mathrm{W}}(\mathrm{conn.})$ are given in Figs. 9 and 10, respectively. For the fit method correlator-reconstruction strategy, we give covariance matrices for results using M_Ω and f_π scale setting in Tables V and VI, respectively, and error budgets for results using f_π scale setting are given in Table VII. Results for the continuum extrapolation BMA using the M_Ω scale for $a_\mu^{ll,\,\mathrm{LD}}(\mathrm{conn.})$ with the fit method are given in Fig. 11. We also give analogous results with each of these three analysis choices varied individually, *i.e.*, using the f_π scale in Fig. 12, for $a_\mu^{ll,\,\mathrm{Full}}(\mathrm{conn.})$ in Fig. 13, and with the bounding method in Fig. 14.

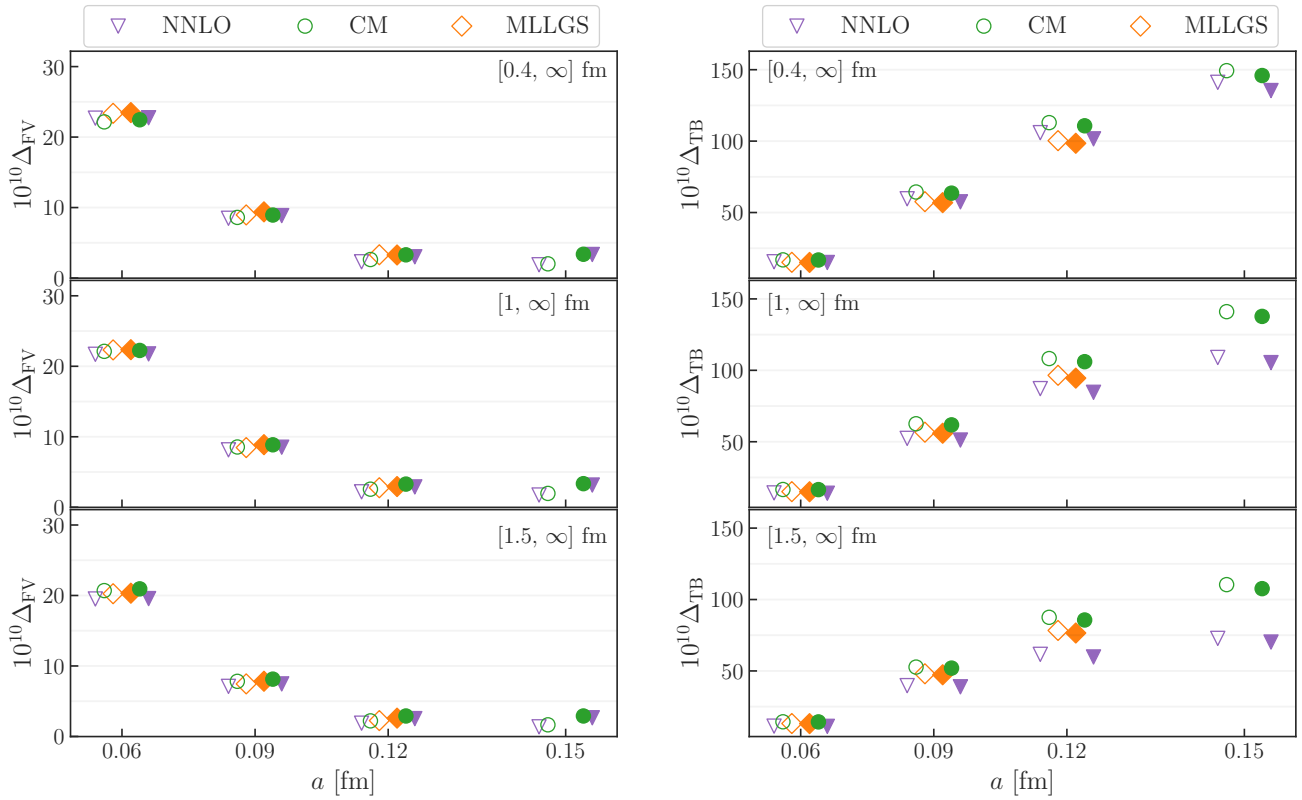

FIG. 8. *Left plot*: FV corrections for each ensemble used in this work. *Right plot*: TB corrections for each ensemble used in this work. The unfilled symbols correspond to the local current and the filled to the one-link.

TABLE IV. Final results for a_μ (in units of 10^{-10}). The first column lists the specific LQC contribution. Columns two and three give results using the fit method (or just raw data in the case of $a_\mu^{ll,\,\rm SD}$(conn.) and $a_\mu^{ll,\,\rm W}$(conn.)) based on scale setting via M_Ω or f_π, respectively. Similarly, columns four and five are results from the bounding method.

	Fit (or raw data)		Bounding	
Contrib.	M_Ω	f_π	M_Ω	f_π
$a_\mu^{ll,\,\rm SD}$	48.119(10)(86)[87]	48.118(11)(85)[86]	—	—
$a_\mu^{ll,\,\rm W}$	206.87(14)(60)[62]	206.89(15)(45)[47]	—	—
$a_\mu^{ll,\,\rm LD}$	401.1(2.3)(3.6)[4.3]	397.4(2.2)(3.2)[3.9]	406.4(3.5)(3.8)[5.2]	402.2(3.4)(3.4)[4.8]
$a_\mu^{ll,\,\rm Full}$	655.1(2.4)(4.5)[5.1]	651.1(2.4)(4.2)[4.8]	660.6(3.7)(5.0)[6.2]	656.2(3.6)(4.7)[5.9]
a_μ^{ll}	656.2(1.9)(4.0)[4.4]	652.4(1.9)(3.5)[4.0]	661.5(3.1)(4.3)[5.3]	657.2(3.1)(3.8)[4.9]

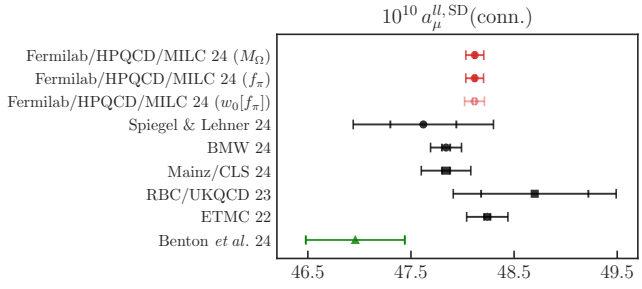

FIG. 9. Comparison of our lattice determinations for $a_\mu^{ll,\,\rm SD}$(conn.) (red circles) labeled "Fermilab/HPQCD/MILC 24 (M_Ω)" and "Fermilab/HPQCD/MILC 24 (f_π)" to our value from [67] (light red circles) labeled "Fermilab/HPQCD/MILC 24 ($w_0[f_\pi]$)" and $n_f = 2+1+1$ (black circles) and $n_f = 2+1$ (black squares) lattice-QCD calculations by Spiegel & Lehner 24 [64], BMW 24 [61], Mainz/CLS 24 [62], RBC/UKQCD 23 [60] and ETMC 22 [57]. The inner error bar shown for our result is from Monte Carlo statistics. Also shown is a data-driven evaluation of $a_\mu^{ll,\,\rm SD}$(conn.) using e^+e^- cross section data (green triangle) by Benton *et al.* 24 [68].

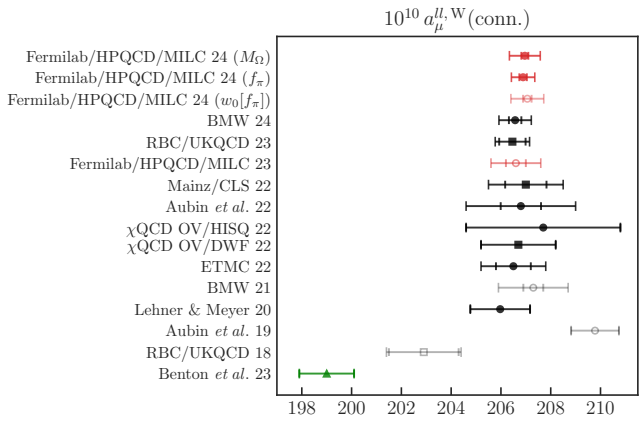

FIG. 10. Comparison of our lattice determinations for $a_\mu^{ll,\mathrm{W}}$(conn.) (red circles) labeled "Fermilab/HPQCD/MILC 24 (M_Ω)" and "Fermilab/HPQCD/MILC 24 (f_π)" with our value from [67] (light red circles) labeled "Fermilab/HPQCD/MILC 24 ($w_0[f_\pi]$)" and $n_f = 2+1+1$ (black circles) and $n_f = 2+1$ (black squares) lattice-QCD calculations by BMW 24 [61], RBC/UKQCD 23 [60], Mainz/CLS 22 [58], Aubin *et al.* 22 [56], χQCD 22 [109], ETMC 22 [57] and Lehner & Meyer 20 [100]. Our previous result, Fermilab/HPQCD/MILC 23, is shown in light red. BMW 21 [55], Aubin *et al.* 19 [101] and RBC/UKQCD 18 [69], shown in gray, have been superseded. The inner error bar shown for our result is from Monte Carlo statistics. Also shown is a data-driven evaluation of $a_\mu^{ll,\mathrm{W}}$(conn.) using e^+e^- cross section data (green triangle) by Benton *et al.* 23 [68, 71].

TABLE V. Correlation matrix for the LQC contributions to the window observables using M_Ω scale setting and (where applicable) the fit method correlator-reconstruction strategy.

	$a_\mu^{ll,\mathrm{SD}}$	$a_\mu^{ll,\mathrm{W}}$	$a_\mu^{ll,\mathrm{LD}}$	a_μ^{ll}
$a_\mu^{ll,\mathrm{SD}}$	1	0.08	0.00	0.01
$a_\mu^{ll,\mathrm{W}}$	0.08	1	0.23	0.21
$a_\mu^{ll,\mathrm{LD}}$	0.00	0.23	1	0.36
$a_\mu^{ll,\mathrm{Full}}$	0.01	0.21	0.36	1.

TABLE VI. Correlation matrix for the LQC contributions to the window observables using f_π scale setting and (where applicable) the fit method correlator-reconstruction strategy.

	$a_\mu^{ll,\mathrm{SD}}$	$a_\mu^{ll,\mathrm{W}}$	$a_\mu^{ll,\mathrm{LD}}$	$a_\mu^{ll,\mathrm{Full}}$
$a_\mu^{ll,\mathrm{SD}}$	1	0.21	0.02	0.03
$a_\mu^{ll,\mathrm{W}}$	0.21	1	0.20	0.14
$a_\mu^{ll,\mathrm{LD}}$	0.02	0.20	1	0.33
$a_\mu^{ll,\mathrm{Full}}$	0.03	0.14	0.33	1

Contrib.	stat., $t_{\min}$	$a\to 0$, Δ_{TB}	Δ_{FV}, Δ_{M_π}	a	Z_V	Total
$a_\mu^{ll,\mathrm{SD}}$	0.010	0.054	—	0.010	0.065	0.086
$a_\mu^{ll,\mathrm{W}}$	0.15	0.18	0.33	0.15	0.19	0.47
$a_\mu^{ll,\mathrm{LD}}$	2.2	2.6	1.5	1.4	0.2	3.9
a_μ^{ll}	2.0	2.7	1.7	1.4	0.3	4.0

TABLE VII. Approximate absolute error budgets (in units of 10^{-10}) for the uncertainties reported in Table IV for the f_π results using the fit method. From left to right, the contributions to the error are Monte Carlo statistics and $t_{\min}$ variation in the correlator fits (where applicable), continuum extrapolation and TB corrections, FV and M_π-mistuning corrections, scale setting, and current renormalization.

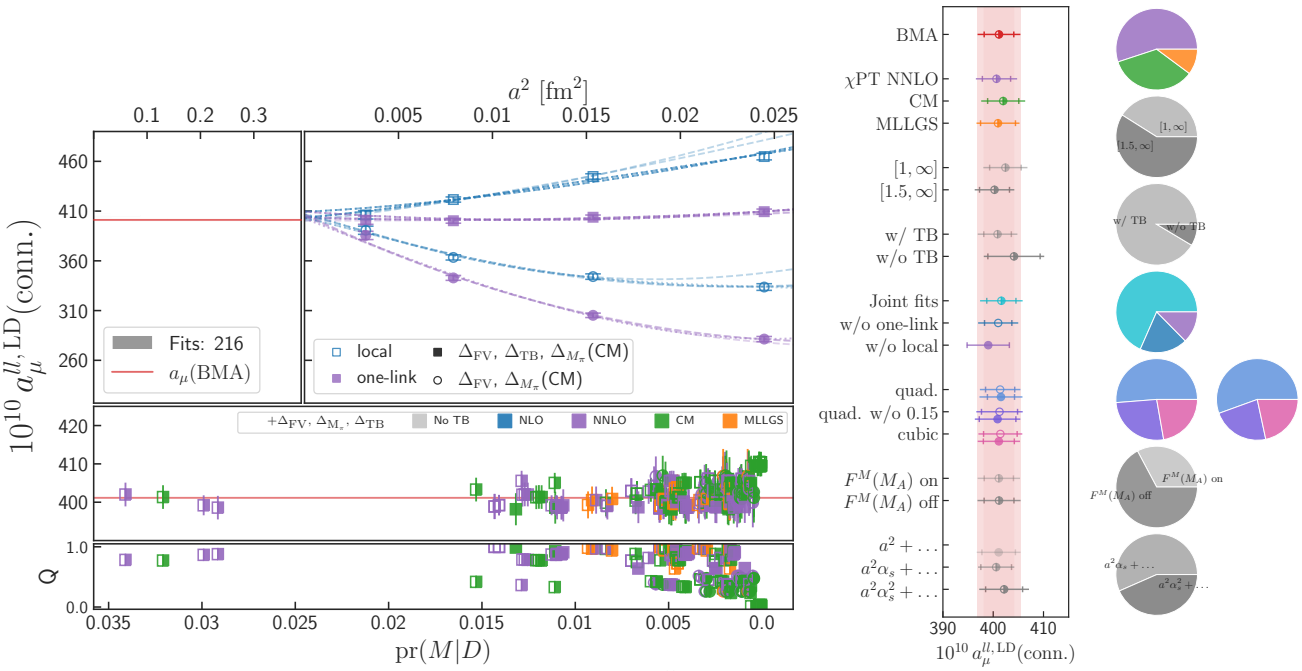

FIG. 11. *Left plot*: Results of the BMA procedure applied to $a_\mu^{ll,\,\mathrm{LD}}(\mathrm{conn.})$ using the fit method for correlator-reconstruction and M_Ω for scale setting. *Upper left panel*: Histogram of all continuum extrapolations used in the BMA weighted by pr$(M|D)$, the inner light-red band includes statistical and parametric errors corresponding to the first term in Eq. (13), while the outer is the total error. *Upper right panel*: The subset of datasets and extrapolations corresponding to correcting the local (blue unfilled) and one-link (purple filled) currents with lattice corrections from the CM correction scheme. Different extrapolations correspond to variations of the fit function and ensembles included. *Lower panels*: The best fits according to the model probability, Eq. (14). The middle panel shows the fit results, where joint fits are indicated with mixed-filled symbols. The bottom one shows the corresponding Q values [110]. In both panels, the correction schemes employed for Δ_{FV}, Δ_{M_π} and Δ_{TB} are indicated by the symbols' color, according to the legend in the middle panel. *Right plot*: Breakdown of the results from the BMA applied to $a_\mu^{ll,\,\mathrm{LD}}(\mathrm{conn.})$. *Left panel*: From top to bottom, the first, main result (BMA) includes all datasets, schemes, and other variations. The next block of results vary the schemes for FV, M_π-mistuning and TB corrections. The next two correspond to different euclidean-time integration regions over which the corrections are computed. Next is a division of all the models into whether TB corrections were applied. The following three are continuum extrapolations to either both currents jointly or one of the currents individually. The next six are subsets with specific continuum fit functions, corresponding to quadratic and cubic, as well as omitting the 0.15 fm ensemble. The unfilled circles correspond to the local current, the filled to the one-link current. The next two correspond to continuum fits with or without the sea-quark-mass–mistuning term. The final three are subsets with differing leading powers of α_s in the fit function where, again, unfilled symbols are the local current and the filled symbols are one-link. The inner error bars on the data points include statistical and parametric errors corresponding to the first term in Eq. (13), while the outer are the total errors. *Right panels*: Pie charts showing the contributions to the BMA corresponding to the groupings in the left panel. The percentages are computed from Eq. (15) for the particular subsets. In the case of the continuum fit function subsets, which are broken up into local and one-link current variations, the left pie-chart corresponds to the local current and the right to the one-link.

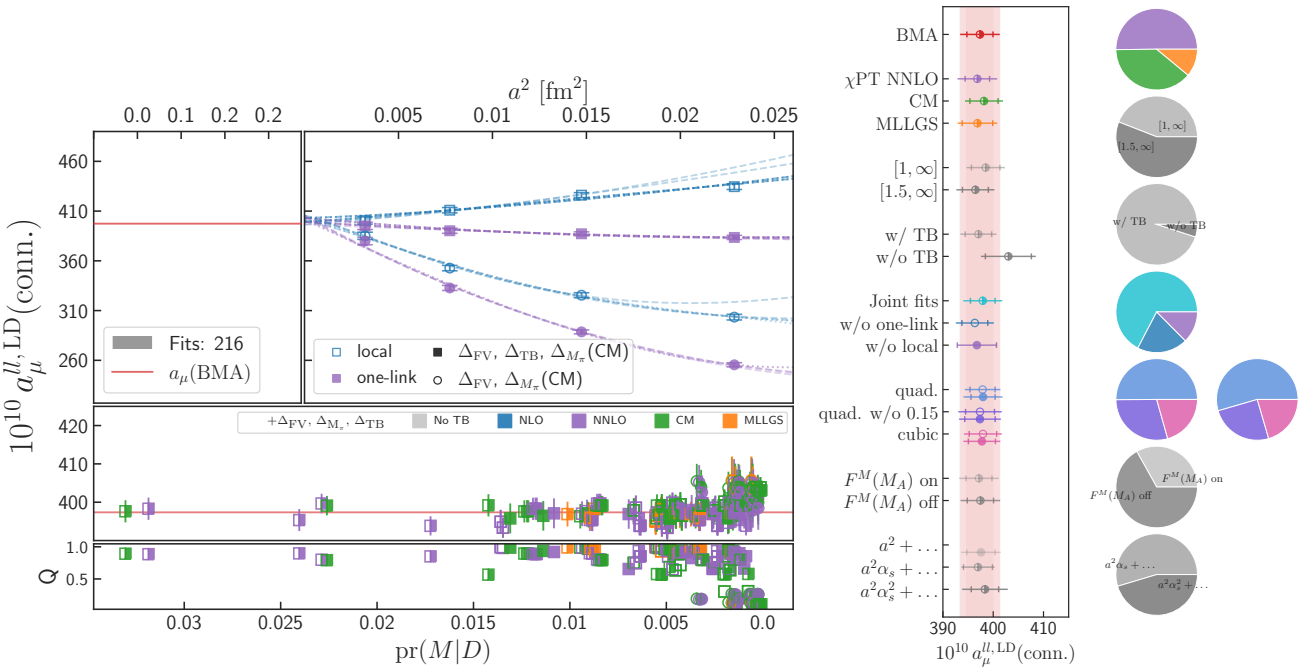

FIG. 12. Results of the BMA procedure applied to $a_\mu^{ll,\,\mathrm{LD}}$(conn.) using the fit method correlator-reconstruction approach and f_π for scale setting. See Fig. 11 for a complete description of the plot. The same axis scale is employed here from that plot.

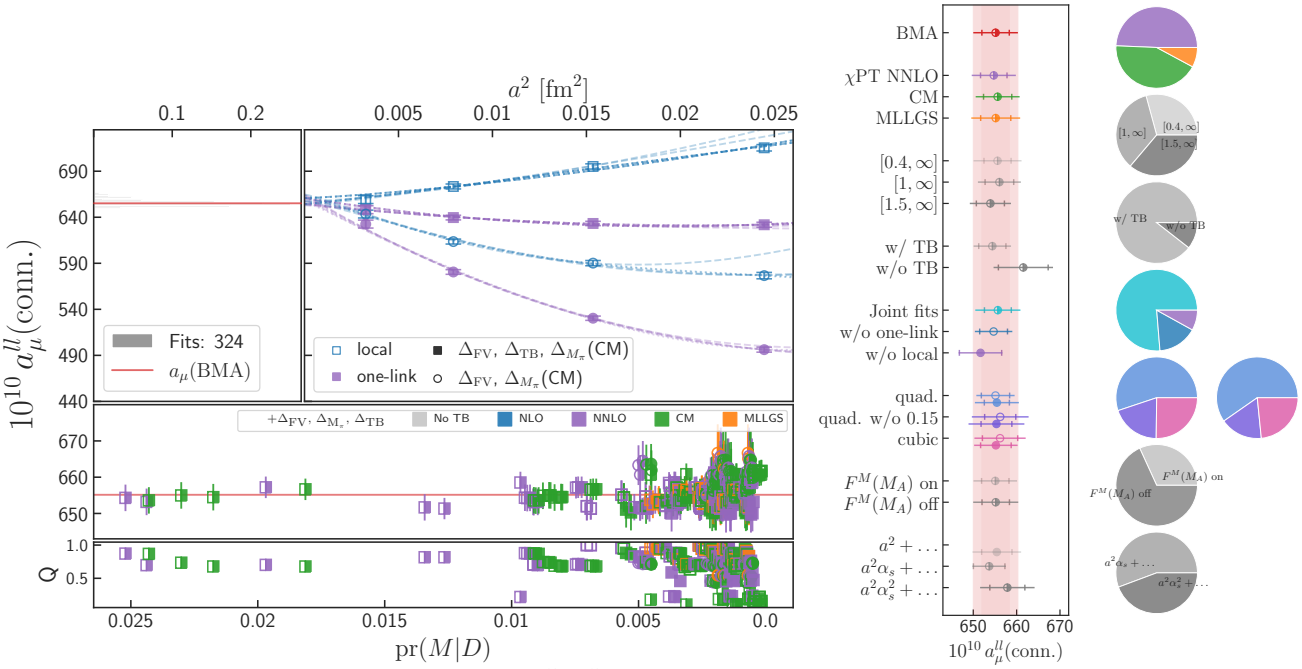

FIG. 13. Results of the BMA procedure applied to $a_\mu^{ll,\,\mathrm{Full}}$(conn.) using the fit method correlator-reconstruction approach and M_Ω for scale setting. See Fig. 11 for a complete description of the plot.

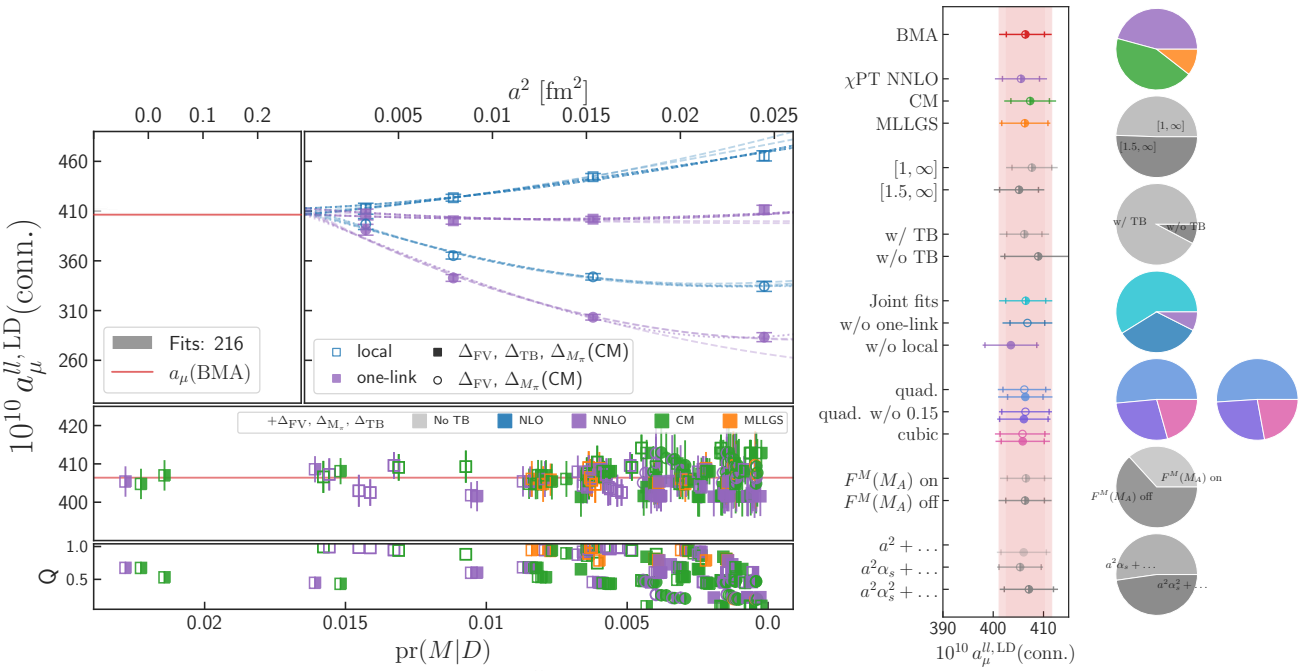

FIG. 14. Results of the BMA procedure applied to $a_\mu^{ll,\,\mathrm{LD}}$(conn.) using the bounding method correlator-reconstruction approach and M_Ω for scale setting. See Fig. 11 for a complete description of the plot. The same axis scale is employed here from that plot.